A tesselation-based model for intensity estimation and laser plasma interactions calculations in three dimensions

A. Colaïtis,[1,2] T. Chapman,[1] D. Strozzi,[1] L. Divol,[1] and P. Michel[1]
[1]*Lawrence Livermore National Laboratory, 7000 East Ave., Livermore, California 94550-9234, USA*
[2]*Laboratory for Laser Energetics, 250 East River Rd, Rochester, New York 14623-1212, USA*

(Received 22 December 2017; accepted 9 March 2018; published online 26 March 2018)

A three-dimensional laser propagation model for computation of laser-plasma interactions is presented. It is focused on indirect drive geometries in inertial confinement fusion and formulated for use at large temporal and spatial scales. A modified tesselation-based estimator and a relaxation scheme are used to estimate the intensity distribution in plasma from geometrical optics rays. Comparisons with reference solutions show that this approach is well-suited to reproduce realistic 3D intensity field distributions of beams smoothed by phase plates. It is shown that the method requires a reduced number of rays compared to traditional rigid-scale intensity estimation. Using this field estimator, we have implemented laser refraction, inverse-bremsstrahlung absorption, and steady-state crossed-beam energy transfer with a linear kinetic model in the numerical code VAMPIRE. Probe beam amplification and laser spot shapes are compared with experimental results and pF3D paraxial simulations. These results are promising for the efficient and accurate computation of laser intensity distributions in holhraums, which is of importance for determining the capsule implosion shape and risks of laser-plasma instabilities such as hot electron generation and backscatter in multi-beam configurations. *Published by AIP Publishing.*
https://doi.org/10.1063/1.5020385

I. INTRODUCTION

Non-linear Laser Plasma Interaction (LPI) processes are key to Inertial Confinement Fusion (ICF) experiments.[1–5] In their presence, the hydrodynamics of targets may be greatly modified: Crossed Beam Energy Transfer (CBET) redistributes laser energy spatially, Stimulated Raman Scattering (SRS) and Stimulated Brillouin Scattering (SBS) lead to losses of laser-target coupling, and SRS and Two Plasmon Decay (TPD) can generate hot-electrons which change the target properties with respect to compression and shock propagation. Despite these prominent effects, few non-linear LPIs are actually accounted for in radiative hydrodynamic codes, thus limiting their predictability.

The difficulty in implementing LPIs at the large temporal and spatial dimensions of fluid codes is essentially a scale problem. ICF and HED experiments on high power lasers such as National Ignition Facility (NIF) or OMEGA involve laser pulses and target dynamics occurring over several tens of nanoseconds and millimeter or centimeter spatial scales. However, LPIs entail a wide range of microscopic processes occurring on sub-ps timescales and sub-μm length-scales. While the fluid scale is correctly described by radiative-hydrodynamic models which allow us to study large plasma volumes on long durations, an accurate description of LPI should in principle require using kinetic models (particle-in-cell and Fokker-Planck), which cannot be used at the full scales of ICF experiments.

The state-of-the-art description of laser propagation on large scales relies on reduced approaches compatible with the performances of modern computers. The most common one is the Ray-Tracing model,[6] which describes laser beams by bundles of needle-like rays following the Geometrical Optics (GO) propagation laws[7] and is characterized by a power density. In situations where collective effects and non-linear couplings are unimportant ($I\lambda^2 \lesssim 5\times10^{13}$ W μm^2/cm^2), GO-based models are sufficiently precise and computationally efficient. They describe the laser refraction and plasma heating due to collisional energy absorption. Conversely, LPI modeling at higher interaction parameters requires knowledge of quantities such as the laser intensity field and the direction of the wavefront, which are not readily accessible from the GO equations.[7] Recent efforts have been made in describing nonlinear LPIs at hydrodynamic scales, notably in the case of inline solvers for CBET,[3,4,8,9] inline models for generation of supra-thermal electrons from TPD and SRS,[10] and post-hoc models for energy deposition of backward propagating SRS light.[11]

At the core of these state-of-the-art techniques lies the description of the laser intensity distribution in plasma and, to a certain extent, the wavefront direction and the wavefield polarization. Notable approaches to estimate these quantities rely on either invoking energy conservation laws on a rigid-scale grid or expanding the ray-based framework by introducing phase terms that describe ray thicknesses.[12] The principal drawback of rigid-scale methods is related to the arbitrary choice of a grid. This is often dictated by hydrodynamic processes and not the position of laser field gradients. Additionally, these methods suffer from poor convergence properties since a sufficient number of rays per cell must be ensured. The limitations of the thick-ray approach lie mainly in the short Rayleigh-range of the Gaussian beamlets it describes, in the difficulty in implementing it in 3D geometries, and in potential parallelization issues on domain-decomposed meshes. In both cases, the accuracy of the reconstructed laser intensity field compared to realistic laser beams is limited unless committing significant computational resources, especially in 3D geometries.

In this paper, we present a novel approach to estimate the laser intensity distribution in plasma in the Geometrical Optics framework. The method is implemented in a new LPI tool called VAMPIRE (VORONOI ADAPTIVE METHOD FOR PROPAGATION AND INTERACTION OF RADIATED ENERGY). It is focused on (i) efficiency with respect to 3D geometries, (ii) accuracy with respect to microscopic reference codes, and (iii) relaxed dependency on the underlying choice of a mesh. The GO framework is presented in Sec. II, alongside the standard rigid-scale estimation method used in most radiative-hydrodynamic codes. We then present our adaptive-scale model in Sec. III. It is compared with reference laser intensity distributions and paraxial solutions of laser propagation. Comparisons to a standard rigid-scale estimator are also shown. We then present in Sec. IV an application of the method to the modeling of CBET. The model is validated in the linear instability regime against theoretical results, and convergence properties with respect to the rigid-scale method are discussed. The model is then validated in the non-linear ("pump-depletion") instability regime against paraxial simulations and experimental results.

II. GEOMETRICAL OPTICS AND RIGID-SCALE ESTIMATION

We briefly recall in this section the Geometrical Optics trajectory and amplitude transport equations. From the latter, we present the inverse Bremsstrahlung based rigid-scale estimator used in most radiative hydrodynamic codes to compute the laser intensity.

A. Trajectory and transport equation

In the absence of laser-plasma instabilities and in the non-relativistic regime, the laser light propagating in plasma undergoes refraction and diffraction and is absorbed through the inverse Bremsstrahlung process. The electromagnetic wave obeys a dispersion relation that limits its propagation up to a critical density $n_c = \epsilon_0\omega^2 m_e/e^2$, where ϵ_0 is the vacuum dielectric constant, ω is the wave frequency, m_e is the electron mass, and e is the electron charge. The refraction of the wave is dictated by gradients in the plasma dielectric function, defined as $\epsilon(\omega) = \epsilon'(\omega) + \imath\epsilon''(\omega) = 1 - (n_e/n_c)[\omega/(\omega + \imath\nu_{\rm IB})]$, with n_e being the electron density, $\nu_{\rm IB}$ a collision frequency for the inverse Bremsstrahlung process, and ϵ' and ϵ'' the real and imaginary parts of ϵ, respectively.

The starting point of Geometrical Optics is the *Helmholtz equation*, obtained from the Maxwell equations assuming monochromatic laser light of frequency ω and either s-polarized (i.e., $\mathbf{E}.\nabla\epsilon = 0$, where $\mathbf{E}$ is the electric field vector) or propagating far from the plasma critical density ($n_e \ll n_c$)

$$\nabla^2 u(\mathbf{r}) + \frac{\omega^2}{c^2}\epsilon(\mathbf{r})u(\mathbf{r}) = 0\,, \tag{1}$$

where u is any component of the wave's electric or magnetic field. Far from the plasma critical density, ϵ can be written as $\epsilon \approx 1 - n_e/n_c(1 + \imath\nu_{\rm IB}/\omega)$. The GO framework is obtained by considering an almost-plane wave ansatz (or WKB) for the field components[7]

$$u(\mathbf{r}) = A(\mathbf{r})\exp[\imath k_0\Phi(\mathbf{r})], \tag{2}$$

where A(r) is an amplitude, Φ is the eikonal or optical path, and $k_0 = \omega/c$ is the free space wavenumber. In the GO framework, it is assumed that A and Φ are real-valued. It is interesting to note that expansion of the method to complex eikonals is the framework of the aforementioned thick-ray approach,[12,13] while extending both terms to complex values is the framework of Complex Geometrical Optics.[14] Both A and Φ are written in the Slowly Varying Envelope Approximation (SVEA), which validity requires that these quantities vary slowly over the wavelength c/ω. It can be shown that this approximation holds far from the critical density and for weakly dissipative media, i.e., for $\epsilon'' \ll \epsilon'$. Inserting the above ansatz in the Helmholtz equation and equating the various terms in inverse powers of $(\imath k)$, we obtain

$$\begin{gathered}(\nabla\Phi)^2 = \epsilon'(\boldsymbol{r})\,,\\ 2\nabla\Phi.\nabla A + A\triangle\Phi + k_0\epsilon'' A = 0\,,\\ \triangle A = 0\,,\end{gathered} \tag{3}$$

where it was assumed that $\epsilon'' \ll \epsilon'$ in agreement with the SVEA. The first equation is the *eikonal equation* and can be solved using the characteristic technique to obtain the GO trajectory equations in Hamiltonian form

$$\frac{d\boldsymbol{r}}{d\tau} = \boldsymbol{p}\,,\quad \frac{d\boldsymbol{p}}{d\tau} = \frac{c^2}{2}\nabla\epsilon'(\boldsymbol{r}) \tag{4}$$

with τ being a real-valued curvilinear coordinate, $\boldsymbol{r}$ the ray position, and $\boldsymbol{p}$ its momentum. The second equation in (3) can be integrated along a ray trajectory to give

$$A(\tau) = A(\tau_0)/\sqrt{\mathcal{J}}\exp\left[-\frac{k_0}{2}\int_{\tau_0}^{\tau}\epsilon''\mathrm{d}\tau'\right], \tag{5}$$

where $\mathcal{J}$ describes the divergence of an infinitesimally thin ray tube around the ray, thus representing the contribution from local density gradients to the amplitude of the ray. The exponential term on the right is simply the inverse Bremsstrahlung damping.

There are two main limitations to this formulation: it is divergent at caustics, where $\mathcal{J}$ goes to zero, and it does not describe the field intensity away from the ray, e.g., there is no radial dependence on A and hence no notion of the ray width and intensity. Despite these limitations, a power can be associated with a GO ray by integrating Eq. (5) along an infinitesimal transverse surface $P(\tau) = \frac{1}{2}c\epsilon_0\int_{S(\tau)}A^2(\tau)\sqrt{1 - n_e(\tau)/n_c}\,\mathrm{d}a$, where $S(\tau)$ is the cross-section of the ray tube at τ. Integrating Eq. (5) and differentiating with respect to the ray parameter τ yield the power conservation equation along a ray trajectory

$$\frac{\mathrm{d}P}{\mathrm{d}\tau} = -\frac{n_e}{n_c}\nu_{\rm IB}P\,. \tag{6}$$

This equation is integrated along the trajectory of GO rays to compute inverse Bremsstrahlung absorption.

B. Rigid-scale inverse-Bremsstrahlung based laser intensity estimation

Assuming constant plasma parameters[33] in a volume V of a mesh cell and assuming the steady-state, the energy conservation equation for the electromagnetic energy density equation can be integrated to obtain the squared electric field $|E|^2$

$$-\Delta P_{\mathrm{abs}} = -\nu_{\mathrm{IB}} \frac{n_e}{n_c} \frac{\epsilon_0}{2} |E|^2 V \tag{7}$$

with ΔP_{abs} being the total power deposited from all rays in that cell, obtained by integrating Eq. (6) along their trajectories.

This formulation essentially consists of binning the collisional absorption from GO rays on a grid to infer the laser intensity. The accuracy and convergence properties of this method are sensitive to (i) the choice of cell size and (ii) the statistical number of rays per cell. The first point implies that the estimator is poorly suited to Lagrangian codes where the cell size is dictated by hydrodynamics and not laser field gradients. This is especially prominent in the laser-generated coronal plasma region where only a few cells typically span from n_c to $n_c/10$. The second point implies poor convergence properties in 3D geometries where the number of cells transverse to the laser propagation is squared from 2D to 3D. The low number of rays per cell will lead to intensity and wavevector fields with holes and large amplitude noise.

In Sec. III, we describe an approach to laser intensity field estimation that does not rely on a grid. This allows us to relax the stringent convergence requirements of usual rigid-scale estimators. Moreover, we show that the method allows for a more realistic laser intensity distribution in plasma.

III. TESSELATION-BASED INTENSITY ESTIMATION

A. Formulation of the model

We describe in this section the formulation of the propagation model. We discuss the beam sampling method used, followed by the field intensity reconstruction and the control of its statistics.

1. Ray distribution

In order to reproduce realistic intensity statistics using the method described here, it is necessary to introduce a random statistical element to the ray distribution. Indeed, for a beam modeled by equally spaced rays, the estimator we describe in Sec. III A 2 would behave differently in homogeneous and inhomogeneous media. It would produce a smooth homogeneous field in the former and an inhomogeneous field in the latter case. We describe here the way in which rays are distributed in VAMPIRE.

Let us consider two planes $\mathcal{P}_L$ and $\mathcal{P}_F$ (for *lens* and *focal*) where the wavefield envelope is known (where the term *envelope* refers to the spatially averaged intensity profile of the beam). We randomly discretize $\mathcal{P}_L$ and $\mathcal{P}_F$ with N geometrical optics rays of the same weight P_i by following the statistics of the beam envelope. As such, the local point density is a direct measure of the field intensity, and the point distribution is a statistical sampling of the underlying field intensity distribution. Rays are randomly connected between the two planes, and their intersection with the entry of the simulation box yields the initial position and vectors of the rays. Constructing beams in this way allows mimicking the envelope intensity variation in-between the lens and the focal plane, which arises from the beam diffraction in homogeneous media. Note that this artificial construction does not reproduce the true diffraction physics. The latter would require the use of Complex Geometrical Optics. Typically for beams at the National Ignition Facility (NIF), the field is a flat-top square in $\mathcal{P}_L$ and an elliptical distribution in $\mathcal{P}_F$, with the form

$$I(x, y) = I_0 \exp\left\{ -\left[\left(\frac{x}{r_x}\right)^2 + \left(\frac{y}{r_y}\right)^2 \right]^{\frac{n_G}{2}} \right\}, \tag{8}$$

where x and y denote the transverse beam coordinates in the plane of interest, r_x and r_y are the $1/e$ beam radius along the x and y directions, respectively, and n_G is the super-Gaussian order.

The plasma parameters (temperature, density, velocity, etc.) are described on a hydrodynamical grid that we will refer to as the *coarse* grid, since its resolution is dictated by the Lagrangian dynamics. The rays initialized following the method described above are propagated in the plasma by solving Eqs. (4) and (6). After tracing of the rays, the refraction and power of the wavefield have been sampled along N discrete curves. Discretizing each curve generates a 3D weighted point distribution from which we will reconstruct the underlying intensity field.

The idea of estimating a field density from a set of discrete points is a well-studied problem in Cosmology,[15–18] where mass density is reconstructed from observed point-mass galaxies. A large variety of field estimators are suited for this problem. Recent studies[19] have highlighted the efficiency of order 1 tesselation based methods[20] compared to other approaches. We now present the implementation of one such estimator to the context of laser intensity estimation in plasma.

2. Volume intensity estimation from ray positions

We consider the Cartesian coordinate system of normalized base vectors $(\mathbf{e}_x, \mathbf{e}_y, \mathbf{e}_z)$. The plane denoted as $\mathcal{P}_z$ constitutes the set of points in $(\mathbf{e}_x, \mathbf{e}_y)$ at coordinate z. The intersection of N rays with $\mathcal{P}_z$ is denoted as $\mathcal{M}_z$. Without the loss of generality, we assume that the wavefield is not propagating parallel to $\mathbf{e}_z$. (If that were the case, the rays may not intersect with the $\mathcal{P}_z$ planes and the estimator would lose accuracy or fail. Note that in that case, one can choose a different privileged axis for the estimator.) Points in $\mathcal{M}_z$ have powers P obtained from the ray-trace step. Intensity estimation can be achieved by decomposing $\mathcal{P}_z$ in a structured and regular mesh of cells and count the occurrences of points in each cell, weighted by P. Such rigid-scale intensity estimators (comparable to that described in Sec. II) tend to have poor convergence properties since they do not adapt to the local point density. With the local point density weighted by the ray powers P being a measure of the local field intensity, it is natural to discretize the plane into an arbitrary mesh of cells from the points $\mathcal{M}_z$ such that the cell size is a measure of the local field density. These cells should cover the entire plane without overlap (which facilitates energy conservation) and be convex polygons (allowing well-defined interpolation within each cell). This concept is the basis of *tesselation-based estimators*.

One such estimator is based on the Voronoi plane tesselation, in which cell edges are equidistant to two points and cell vertices are equidistant to three or more points (see Fig. 1). These cells are called *Voronoi cells*. In the case of the Voronoi estimator, the generator points of the Voronoi diagram are the points $\mathcal{M}_z$. The field intensity at a given point i is then estimated as $I_i = P_i/\mathcal{A}_i^V$, where $\mathcal{A}_i^V$ is the area of the Voronoi cell i. Energy conservation is ensured by imposing that the 2D integral of the reconstructed intensity field is equal to the sum of the power values at the N points. A sufficient condition to ensure this energy conservation is to assume a constant field intensity in each Voronoi Cell. Since the reconstructed field is discontinuous at the cell interfaces, this method is termed order 0 estimator. Order 1 field reconstruction is obtained by tesselating $\mathcal{M}_z$ to form a Delaunay Triangulation. In this approach, each point is the vertex of several triangles and no generator point is contained in any circumcircles of the triangles. Each point i is associated with a Contiguous Voronoi Cell, which is the union of triangles sharing i as a common vertex. The field intensity at a point i is then estimated by $I_i = P_i/(3\mathcal{A}_i^C)$, where $\mathcal{A}_i^C$ is the area of the Contiguous Voronoi Cell i and the factor 3 follows from energy conservation in 2 dimensions.[20] This approach, associated with a Delaunay interpolation method described below, is termed Delaunay Triangulation Field Estimation (DTFE).

In our particular case, the DTFE must be corrected for the angle formed between the local k-vector of the wavefield and the reference axis chosen to sample the field (here $\mathbf{e}_z$). This can be understood with a simple example: considering a flat-top beam propagating at an angle θ with respect to $\mathbf{e}_z$, the peak reconstructed intensity in any slice of the 3D volume should be the same. However, the local ray density in an arbitrary intersecting plane $\mathcal{P}$ will be different depending on the choice of the plane orientation, with the highest density for a plane orthogonal to the beam propagation. We compensate for this bias by correcting the intensity estimated at each point with a factor depending on the local wavefield angle with respect to the orthogonal axis to plane $\mathcal{P}$

$$I_i = P_i/\left[3\mathcal{A}_i^C \cos(\Theta_i)\right], \tag{9}$$

where the mean wavefield angle Θ_i with respect to $\mathbf{e}_z$ is defined in the Contiguous Voronoi Cell i (associated with ray i) as

$$\cos(\Theta_i) = \left(\frac{\Sigma_{j\in\mathcal{N}_i}\hat{\mathbf{k}}_j P_j}{\Sigma_{j\in\mathcal{N}_i}P_j}\right).\mathbf{e}_z \tag{10}$$

with $\hat{\mathbf{k}}_j$ being the propagation vector of ray j normalized to 1 and $\mathcal{N}_i$ is the set of points comprising the neighbors of i (i.e., vertices of the Contiguous Voronoi Cell), including i itself.

Because the Delaunay Triangulation only involves regular polygons (i.e., triangles in 2 dimensions), it is natural to describe the sub-grid field distribution by functions of the form $I(x,y) = Ax + By + C$. Proceeding in that way yields a reconstructed field that is $\mathcal{C}^0$ in $\mathcal{P}_z$. The estimated field at points $\mathcal{M}_z$ is interpolated inside the Delaunay triangles and sampled onto a high-resolution regular mesh in $\mathcal{P}_z$. The latter is then binned onto a lower resolution grid that can be used for purposes of interaction with other beams (see Sec. IV). In order to avoid spurious effects, we only interpolate within the convex hull of the beam envelope in $\mathcal{P}_z$. This provides a sharp cutoff between cells within the envelope and the rest of the coarse grid. This sharp cutoff is necessary to describe intensity-weighted k-vector fields and intensity-weighted frequency fields on the edge of the beams.

The estimation procedure is repeated in N_z planes along the z-axis to obtain a field distribution that covers the 3D simulation volume. This method is particularly well adapted to holhraums since the laser light from a given beam never turns back with respect to the revolution axis of the holhraum. Counter-propagating laser light is simply accounted for by varying the privileged axis or the discretization direction.

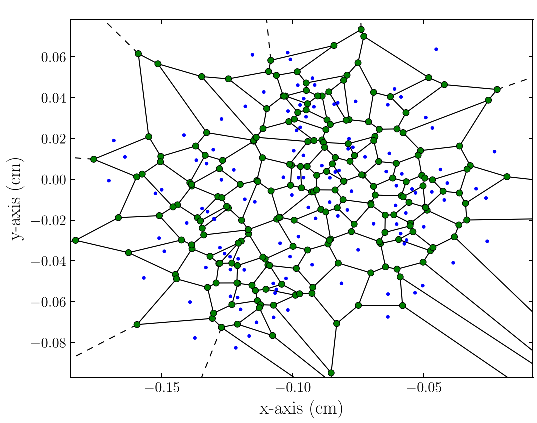

FIG. 1. Illustration of a Voronoi diagram constructed from a set of generator points (blue)—in our case, the geometrical optics rays' positions. Voronoi cell edges are shown in black and cell vertices in green.

3. Relaxation of the reconstructed statistics

By adapting to the local point density, the DTFE is particularly sensitive to gradients. As such it is also sensitive to noise in the point statistics. In our case, the noise originates from the way the laser beam is randomly discretized from GO rays (see Sec. III A 1). While this noise can be suppressed by using a very high number of rays per beam, the smooth reconstructed field would not be representative of a realistic intensity distribution. Indeed, laser beams in high power laser systems are transformed by phase plates which induce fine scale intensity fluctuations called speckles. As such, it is advantageous to use the sensitivity of the DTFE to statistical noise to (i) reproduce a fine scale intensity statistic relevant to the problem and (ii) use a low number of rays per beam.

In order to control the high-intensity tail of the reconstructed intensity distribution, we implement an adaptive-scale relaxation scheme also based on plane tesselation.[21] Essentially, the position of the GO rays $\mathcal{M}_z$ in $\mathcal{P}_z$ is relaxed toward a point distribution $\mathcal{M}_z^{\rm CVT}$ that would generate a Centroidal Voronoi Tesselation (CVT), i.e., a Voronoi diagram for which the generator points are also centers of mass. Note that the point relaxation only concerns the intensity estimation step, and the actual position of the ray intersection with $\mathcal{P}_z$ is not changed in terms of wavefield propagation. This tesselation-based method is different from fixed-kernel based smoothing algorithms in that it adapts to the local sample density.

The point relaxation is achieved by minimizing a merit function (so-called Lloyd iterations)

$$\chi = \frac{1}{N}\left(\sum_{i=1}^{N}\alpha||\mathbf{p}_i - \mathbf{p}_i^*||^2 + (1-\alpha)||\mathbf{p}_i - \mathbf{p}_i^0||^2\right) \qquad (11)$$

with $\mathbf{p}_i$ being the current generator site positions, $\mathbf{p}_i^*$ the current center of mass positions, and $\mathbf{p}_i^0 \in \mathcal{M}_z$ the original generator site positions. The α parameter allows us to control the final distribution between a pure DTFE ($\alpha = 0$) and a pure CVT ($\alpha = 1$). Convergence of the relaxation iteration is achieved when subsequent iterations do not change the generator site positions significantly. For $\alpha \notin \{0, 1\}$, the method is called Penalized-CVT (PCVT) since the relaxed distribution is not fully a CVT.

The definition of a center of mass $\mathbf{p}_i^*$ for Voronoi Cells implies that the Voronoi diagram must be bound (i.e., not branching to infinity). For that purpose, the initial set of points $\mathcal{M}_z$ is extended to $\hat{\mathcal{M}}_z$ using virtual rays obtained by symmetrizing the points on the convex hull of $\mathcal{M}_z$ along the base vectors $(-\mathbf{e}_x, \mathbf{e}_x)$ and $(-\mathbf{e}_y, \mathbf{e}_y)$ (see Fig. 2). The extended set of generators $\hat{\mathcal{M}}_z$ is relaxed toward the CVT, and the resulting point set is cropped to the original convex hull of $\mathcal{M}_z$. These steps ensure that the beam does not spread outside of its initial envelope with the Lloyds iterations.

While the PCVT relaxation provides some control on the intensity statistics, one must note that the field estimated from an $\alpha = 1$ CVT is not entirely smooth, as illustrated in Fig. 3. Given an initial distribution [Fig. 3(a)], the corresponding sampled statistical distribution [Fig. 3(d)] reconstructed by DTFE yields a field with the correct large-scale variations but with small scale statistics [Fig. 3(b)]. Regularizing the point distribution toward a CVT [Fig. 3(e)] allows us to reproduce a smoother field which still contains information on small scale structures [Fig. 3(c)].

4. Scheme parallelization

As mentioned in the introduction, thick-ray based methods are more challenging to parallelize in 3D geometries on fully domain-decomposed meshes. Indeed, in domain-decomposed ray-tracing schemes, many communications between processes are required when the intensity in a given mesh cell is no longer a function of the rays in that mesh cell only. The same issue arises in the DTFE-PCVT reconstruction technique presented here. However, significant parallelization opportunities remain: the Geometrical Optics step of the estimation can be ran in a domain-decomposed mesh, each beam can be treated separately, and the many Delaunay Triangulations required for each beam and each $\mathcal{P}_z$ can be ran independently.

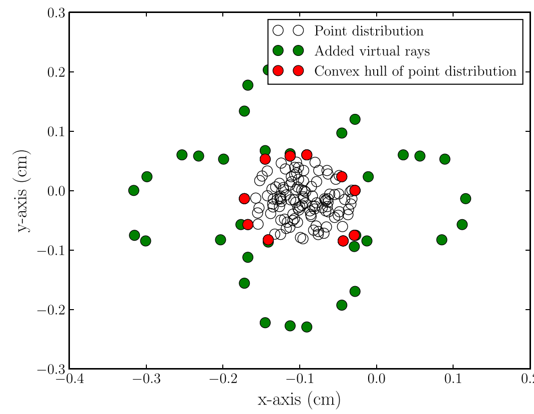

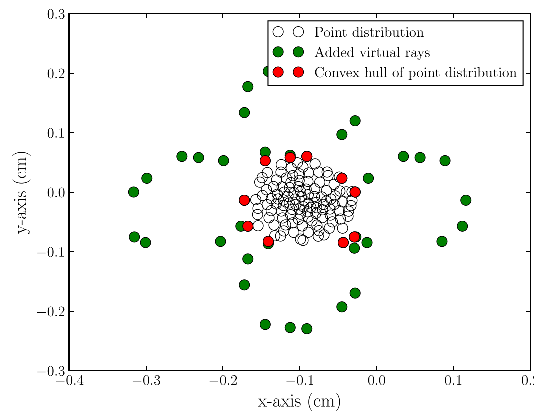

FIG. 2. Generator point distributions used for the PCVT algorithm, for [top] the initial points and [bottom] the relaxed points. The convex hull of $\mathcal{M}_z$ is shown as red dots. Points in $\mathcal{M}_z$ and $\mathcal{M}_z^{\rm CVT}$ are shown as empty and red dots. The virtual points introduced to generate a bound diagram for $\mathcal{M}_z$ and $\mathcal{M}_z^{\rm CVT}$ are shown as green dots. This example uses 30 generator points in $\mathcal{M}_z$, and convergence to $\alpha = 1$ was achieved after 3 Lloyds iterations.

B. Comparison to reference solutions

Basic properties of the reconstructed field are now compared with those of reference solutions of laser propagation. First, the sensitivity of the reconstructed field to the number of rays and choice of the relaxation parameter is studied. The parameters considered for the comparison are the beam envelope intensity, intensity distribution, and speckle size. For the beam envelope, we consider the particular case of NIF beams. Second, the propagation model is briefly compared with a paraxial solution for the case of a beam at perpendicular incidence on a parabolic density gradient. This is a relevant situation for laser beams propagating in indirect-drive ICF.

1. Intensity envelope and statistics

Phaseplates employed in high-power laser systems work by spatially varying the phase of the laser field at the final

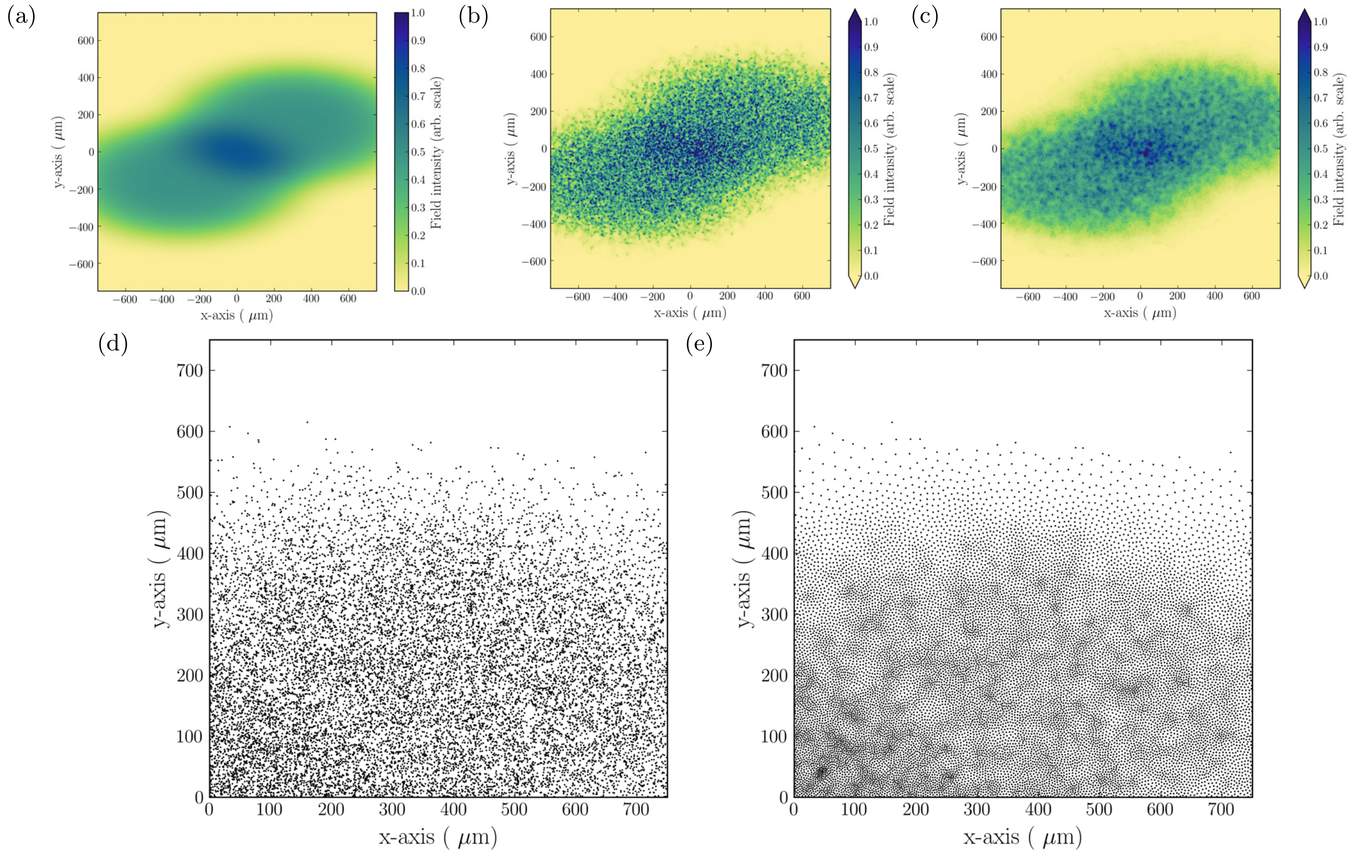

FIG. 3. Illustration of the DTFE-PCVT reconstruction technique for a smooth initial field (a). Generator point positions and reconstructed fields with (b) $\alpha = 0$ and (c) $\alpha = 1$. [Bottom] plots show the generator point positions for the upper right corner of the field, for (d) $\alpha = 0$ and (e) $\alpha = 1$.

focusing optics, thus making the beam interfere with itself in the far field. The characteristic spatial scales of the laser spot in the focal plane of such smoothed beams are dictated by the size of the phase variations in the phase plate and the full beam aperture. This process produces beams with well characterized small scale features and reproducible intensity envelopes. The measured field amplitude for a NIF outer-beam at the phaseplate is shown in Fig. 4 [left]. The corresponding intensity distribution in the focal plane, shown in Fig. 4 [right], is obtained by Fourier Transform of the field amplitude in the near field. The beam envelope parameters are obtained by fitting the focal plane intensity distribution to an elliptical profile of the same form as Eq. (8). For a power of 1 TW, we obtain $I_0 = 5.46 \times 10^{13}$ W/cm^2, $r_x = 679.8\ \mu$m, $r_y = 952.7\ \mu$m, and $n_G = 8.16$.

For the DTFE model, the near field ray statistical distribution is set to a flat-top square of 0.38 m in edge length (see Sec. III A 1 for details on the sampling method). The far-field distribution is set to a super-Gaussian ellipse [Eq. (8)] whose parameters are those of the Fourier Transform fitted solution. The convergence of the DTFE-PCVT estimated intensity field in the focal plane with the number of rays and

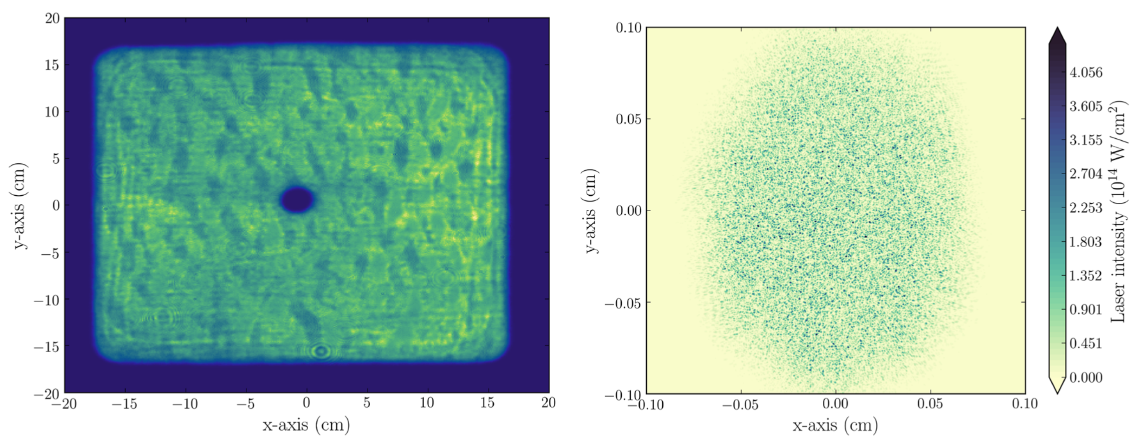

FIG. 4. [Left] field amplitude after a typical outer-beam NIF phaseplate (arb. scale). [Right] corresponding intensity distribution in the focal plane (10^{14} W/cm^2) for a total power of 1 TW.

the choice of the relaxation parameter is shown in Fig. 5. Since the sampling process relies on a statistical method, this convergence is studied over many statistical realizations and the results are shown for both the average and the standard deviation. It is found that the DTFE-PCVT method allows us to accurately reconstruct the large-scale beam parameters. Asymptotic convergence is found for any value of α from 2500 rays. The error is below 1% for the beam radius and envelope intensity and up to 10% for the super-Gaussian order n_G, depending on the choice of α. In general, α is found to only impact significantly the super-Gaussian order, with higher errors for stronger relaxations. The ray position relaxation at high α is more prominent in areas of weak ray density, e.g., in the wings of the beam, where the super-Gaussian fit is most sensitive. Although as low as 1000 rays with $\alpha \leq 0.25$ yield average reconstructed parameters with low errors, the random realization dependency, especially on n_G, becomes significant. As a general rule, it is found that at least 2000 rays per beam with $\alpha \leq 0.25$ are warranted. While a rigid-scale intensity estimator requires a minimum number of rays per cells to converge (e.g., $\sim$10 for CBET applications), this condition is relaxed here: the intensity profile of the beam is constructed from the rays themselves independent of the choice of an underlying grid.

As discussed earlier, the DTFE-PCVT approach produces small-scale intensity variations due to its sensitivity to statistical noise. The characteristic scale of these variations is obtained by fitting a 2D Gaussian distribution to the cross-correlated intensity field. For NIF beams, the $1/e$ speckle radius is $\sim 7\,\mu$m and the intensity field follows an exponential distribution of the form $P(I) \propto \exp(-I/\langle I \rangle)/\langle I \rangle$.[22,23] The intensity distribution and speckle radius generated by the DTFE-PCVT are compared with the reference solution in Fig. 6. In terms of intensity distribution alone, the field reconstruction is found to bracket the reference solution for $\simeq$0.04 and 0.16 rays per transverse cell and $\alpha \in [0, 0.125]$. For a typical $200 \times 200 \times 200$ mesh, these parameters are compatible with the convergence requirements presented earlier. The slope of the intensity distribution tail is controlled by both α and the number of rays. The higher these two parameters are, the smoother the reconstructed field is, with a higher sensitivity to the choice of α. In comparison, the rigid-scale reconstruction technique requires a large number of rays to avoid holes in the reconstructed field and as such produces a distribution centered around the average intensity with a greatly underestimated tail.

In terms of characteristic scale of the intensity variations, larger values of α lead to larger intensity structures and hence larger speckle sizes. Conversely, using more rays leads to a smaller spatial scale for the intensity variations and hence a smaller speckle size. Without relaxation, the modeled speckle size varies from 6 times the reference size to about 2, using 1000 and 4000 rays/cell, respectively. These results show that the method does not simultaneously reproduce the intensity distribution and the speckle size since the parameter range mentioned above produces speckles of about 4–5 times the real speckle size.

In practice, numerical grids used in large-scale propagation models are too coarse to resolve the speckles. The DTFE-PCVT reproduces the correct intensity distribution with larger speckles and hence on coarser grids. The over-estimated speckle radius may be a problem for problems where the gain per speckle is high. For most applications related to CBET in indirect-drive ICF, the speckles are not

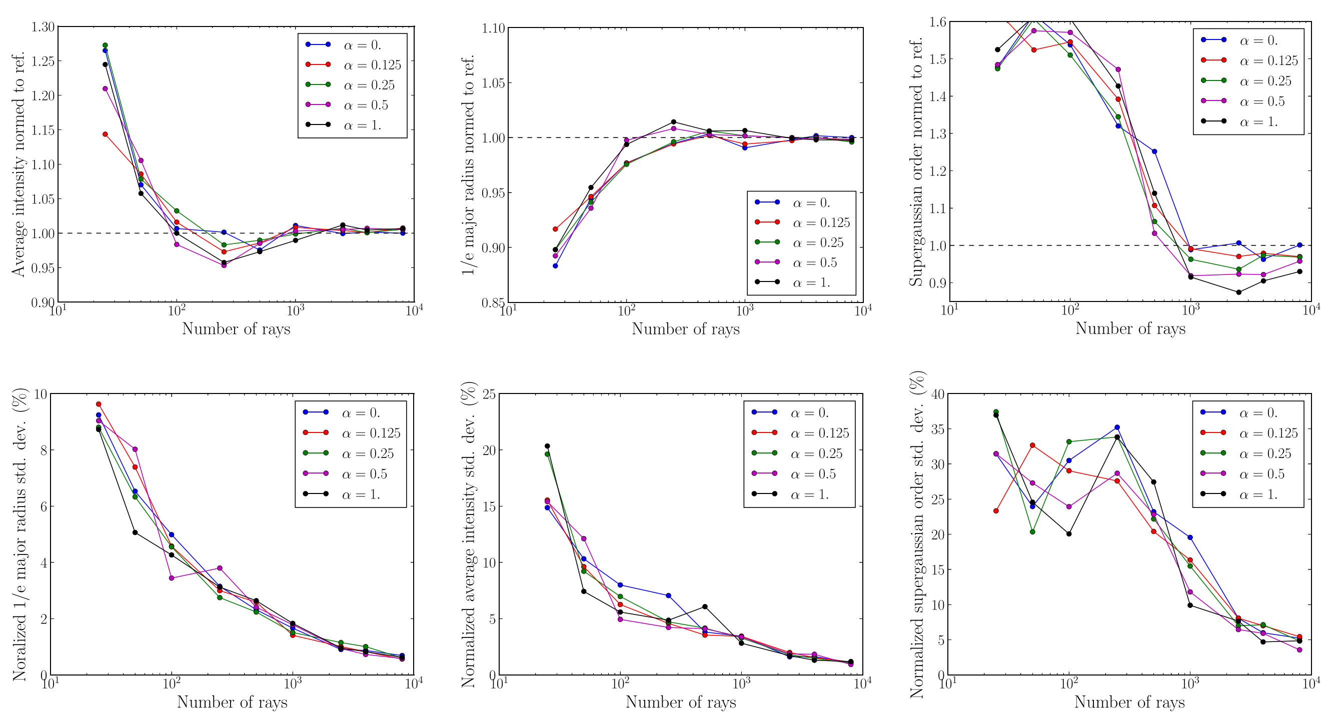

FIG. 5. Dependence of the reconstructed beam envelope parameters ([Left] average intensity, [middle] beam major radius at $1/e$, and [right] supergaussian exponent) on the relaxation parameter $\alpha \in [0, 1]$ and the number of rays $\in [25, 8000]$. The values are normalized to their reference given by the Paraxial solution. [Top] figures show the average reconstructed value over 30 realizations, and [bottom] figures show the associated standard deviation.

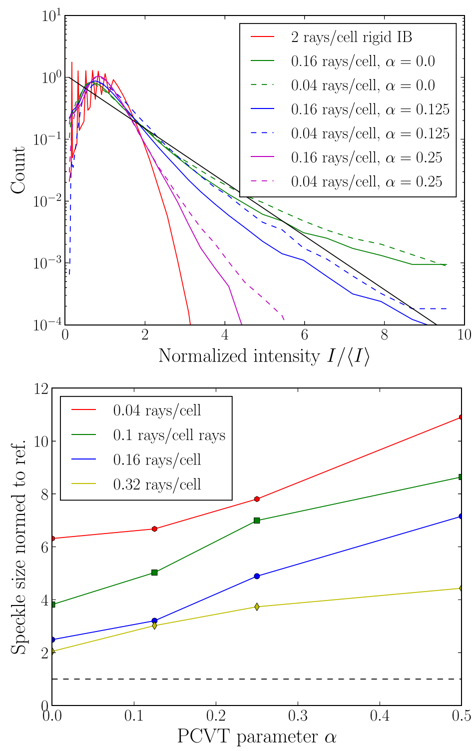

FIG. 6. [Top] field distribution of a phaseplate smoothed NIF beam as a function of intensity normalized to the average intensity. The reference solution $P(I) \propto \frac{\exp(-I/\langle I \rangle)}{\langle I \rangle}$ is given in black. The rigid-scale inverse Bremsstrahlung intensity estimation is shown in red for $\simeq 2$ rays/cell (50k rays). Simulations with a lower number of rays lead to prominent void regions inside the beam, e.g., part of the plasma that would not be covered by the laser field. The DTFE reconstructions for 0.04 and 0.16 rays/cell (1k and 4k rays, respectively) and three values of the relaxation parameters are shown as green, blue, and magenta lines. [Bottom] normalized characteristic spatial scale of the intensity variations as a function of relaxation parameter for the DTFE reconstruction technique.

thought to play an important role compared to the average intensity since the gain over a speckle length is small.[24] In contrast, to properly model an instability near its threshold, accurate speckle modeling is important.[25] For most cases of interest here, it is sufficient to use as low as $\simeq$0.04 rays per transverse cell or 2000 rays (whichever is higher) with $\alpha \leq 0.25$ and large speckles to allow for efficient 3D propagation of the beam with correct large-scale envelope parameters and satisfying intensity distribution.

2. Propagation in a parabolic density gradient

We now consider the case of inhomogeneous media, in which the beam undergoes refraction on density gradients. Simple energy conservation arguments (see Sec. II A) show that refraction causes the local increase and decrease in the laser intensity, which must be accounted for by the propagation model. In the particular case of indirect-drive ICF, beams typically propagate in a weakly inhomogeneous plasma in the laser entrance hole and reach the holhraum wall at an angle. The wall material expands due to the heating by inverse Bremsstrahlung and can, for simple test-case purposes, be represented with a parabolic density profile. The propagation model is now compared with a reference solution obtained with a Paraxial wave solver.

A NIF-like beam is initialized propagating perpendicular to a density gradient of parabolic shape on its left side and constant density on its right side. The density profile is smoothly matched to vacuum on the input side of the beam. The laser light propagating in the density gradient refracts towards the beam center at various rates and creates an intensity enhancement. Comparison of the results obtains with the DTFE-PCVT and Paraxial approaches is shown in Fig. 7. The DTFE-PCVT reproduces the beam turning at the correct rate. This could be expected given that the trajectory equations of Geometrical Optics contain the refraction component of the Paraxial approach. As such, the DTFE-PCVT also reproduces the intensity enhancement due to the local field refraction, as seen by comparing intensity profiles at the output of the simulation box. Note that this test is provided as verification of the DTFE-PCVT estimation scheme, as this effect would also be obtained with rigid-scale estimation with a higher number of rays. However, in regions where refraction induces beam spraying (e.g., after reflection on the wall in indirect-drive geometries), the performances of the latter drop dramatically.

IV. CROSSED-BEAM ENERGY TRANSFER

The VAMPIRE code implements the entire propagation model described in Sec. III. It allows access to the laser intensity at any point in the plasma independent of the underlying choice of hydrodynamic grid. A direct application of the propagation model is the implementation of a Crossed Beam Energy Transfer model to describe the physics of energy exchange between beams crossing in a plasma. We now describe the CBET model, its formulation in VAMPIRE, and its comparison to theoretical and experimental results.

A. Equations of the model

The coupled mode equations for plane waves interacting in the steady state can be written in the following form:[26]

$$\partial_z I_n = -(\kappa_n + \Gamma_n) I_n, \qquad \Gamma_n = \sum_{i \neq n} \frac{g_{ni}}{\omega_i} I_i \tag{12}$$

with I_n being the intensity of wave n, κ_n the inverse Bremsstrahlung absorption rate for wave n, g_{ni} the coupling coefficient between waves n and i, and I_i the intensity of wave i. Here, the z subscript refers to the axis of propagation of wave n. Written in this non-symmetric form, there is a part of energy that is transferred to the ion acoustic wave $p_{ni}^{\mathrm{IAW}} = \frac{\omega_{ni}^{\mathrm{IAW}}}{\omega_n \omega_i} g_{ni} I_n I_i$. It is useful to transcribe this equation in terms of ray power in the framework of GO. This is done by performing a transverse surface integral of I_n on the cross-section of the elementary ray tubes associated with each ray (see Sec. II A) and allow us to swap I_n for the ray power P_n in Eq. (12). The CBET coupling coefficient Γ_n is computed by summing the independent contributions of all other beams, with the coupling term[27]

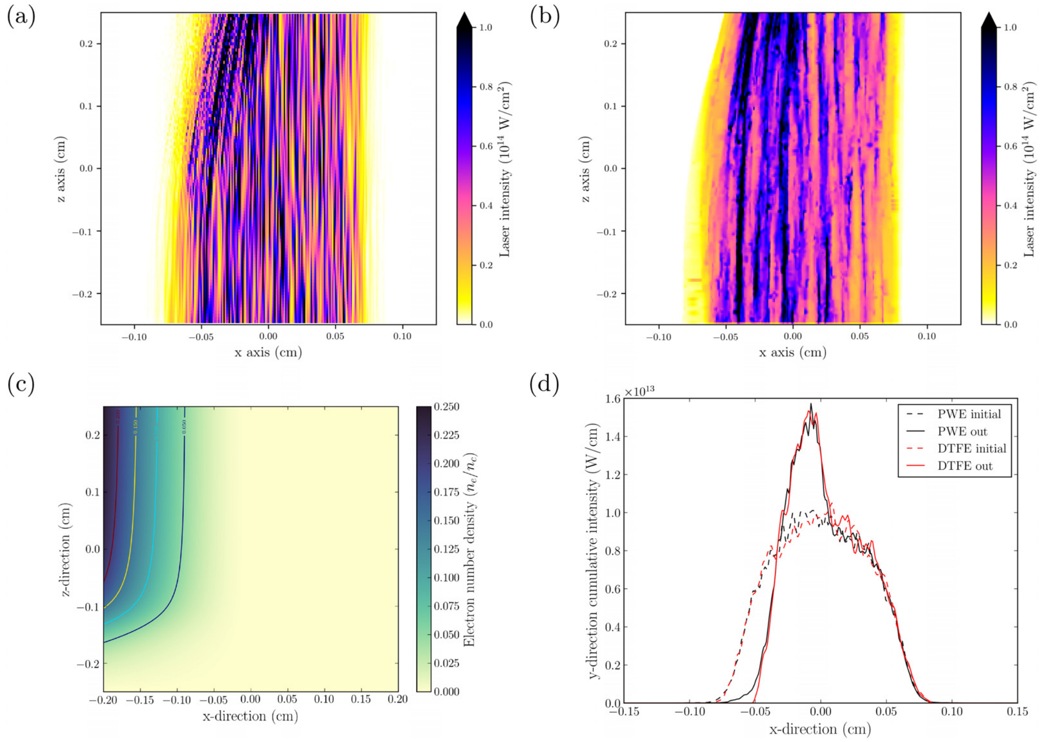

FIG. 7. [Top] Intensity field of a phaseplate-smoothed NIF beam propagating in a semi-parabolic density profile, for (a) the paraxial solution and (b) the DTFE-PCVT solution with 5000 rays and $\alpha = 0.25$. The beam is propagating in the positive z direction. (c) density profile used in the simulation: semi-parabolic in the x-direction, constant in the y-direction, and constant and smoothly matched to vacuum in the z-direction. The slice in the 3D simulation is taken in the mid-plane of the y-direction. (d) cumulative intensity in the y-direction as a function of x ($C_y(x) = \int_{-\infty}^{+\infty} I(x, y, z_0)\mathrm{d}y$) at the input (dashed line) and output (solid line) of the simulation box, respectively. The Paraxial Wave Equation solution (denoted PWE) is in black and the DTFE-PCVT solution in red.

$$
\begin{aligned}
g_{ni} &= \frac{2\pi r_e}{m_e c^2}\frac{k_{s,ni}^2}{k_n k_i}\Im\left(\frac{\chi_{e,ni}(1+\chi_{I,ni})}{1+\chi_{e,ni}+\chi_{I,ni}}\right)\zeta_{ni}\,,\\
\chi_{e,ni} &= -\frac{1}{2k_{s,ni}^2\lambda_{De}^2}Z'\left(\frac{\omega_{s,ni}-\mathbf{k}_{s,ni}.\mathbf{u}}{k_{s,ni}v_{Te}\sqrt{2}}\right),\\
\chi_{I,ni} &= -\sum_j^{\text{species}}\frac{1}{2k_{s,ni}^2\lambda_{Dj}^2}Z'\left(\frac{\omega_{s,ni}-\mathbf{k}_{s,ni}.\mathbf{u}}{k_{s,ni}v_{Tj}\sqrt{2}}\right)
\end{aligned}
\tag{13}
$$

with $\mathbf{k}_{s,ni} = \mathbf{k}_n - \mathbf{k}_i$ being the grating wavevector, $k_s = |\mathbf{k}_s|$, $\omega_{s,ni} = \omega_n - \omega_i$ the grating pulsation, $\mathbf{u}$ the flow velocity vector, r_e the classical electron radius, Z' the derivative of the plasma dispersion function,[34] v_{Tj} the thermal velocity of species j, and ζ_{ni} the polarization coefficient for the two interacting waves. For two unpolarized lasers crossing at angle θ_{ni}, $\zeta_{ni} = (1+\cos^2\theta_{ni})/4$. For two linearly polarized lasers with an angle Θ_{ni} between their polarization vectors at the point of crossing, $\zeta_{ni} = \cos^2\Theta_{ni}$. Note that in this formulation, we assume that the polarization is fixed along the propagation of the beam. This is valid as long as refraction is small prior to and inside the CBET region, and the CBET operates in modest gains ($G \leq 1$) so that it does not turn the field polarization.

The CBET equations (12) have been implemented in VAMPIRE (see App. A for the details on the numerical formulation). We now compare the model with the results from kinetic theory in the linear regime.

B. Comparison to kinetic theory for linear gains

We consider the case of CBET between two beams in the linear regime. The 3D model results are compared with reference gains computed with the LIP code[28] in 1D and with the inline model[11,35] implemented in HYDRA[29] in 3D. The latter relies on the same starting equations for CBET (12) but uses the rigid-scale estimator described in Sec. II. We consider two 3ω flat-top beams interacting at 25° in a homogeneous plasma, with aligned polarizations and an infinite f-number. The plasma is either fully ionized C_5H_{12} at $n_e = 0.15n_c$ or fully ionized He plasma at $n_e = 0.02n_c$. Temperatures are set to $T_e = 1.8$ keV and $T_i = 0.3$ keV. The plasma extends for 0.6 cm along the common direction of propagation of the beams. C_5H_{12} plasma parameters are relevant to conditions presented in Sec. IV C. The He case is considered for its sharp resonance. The pump and seed intensities are set to $I_{\text{pump}} = 6.7\times10^{13}$ W/cm^2 and $I_{\text{seed}} = 10^{-10} I_{\text{pump}}$, respectively. Inverse Bremsstrahlung absorption is turned off. In this configuration, there are no 3D inhomogeneity effects, no finite aperture effects, no finite interaction length effects, no laser absorption, and no pump depletion, and thus, the instability operates in the linear regime. The wavelength detuning between the beams is varied in the [0, 3.5] Å range, and the gain exponent is obtained from the input and output intensity profiles.

The gain curves obtained in both 3D models are compared with the 1D reference in Figs. 8(a) and 8(b). Both models reproduce the theoretical linear gains in the two plasma cases. Comparing the convergence properties of both approaches is not relevant since this would reduce to a measure of the model's ability to produce smooth 1D beams in 3D. However, it is interesting to test the relative accuracy of the two approaches. A comparison of the average gain error is shown in Fig. 8(c), where the average error $\hat{E}$ is defined as

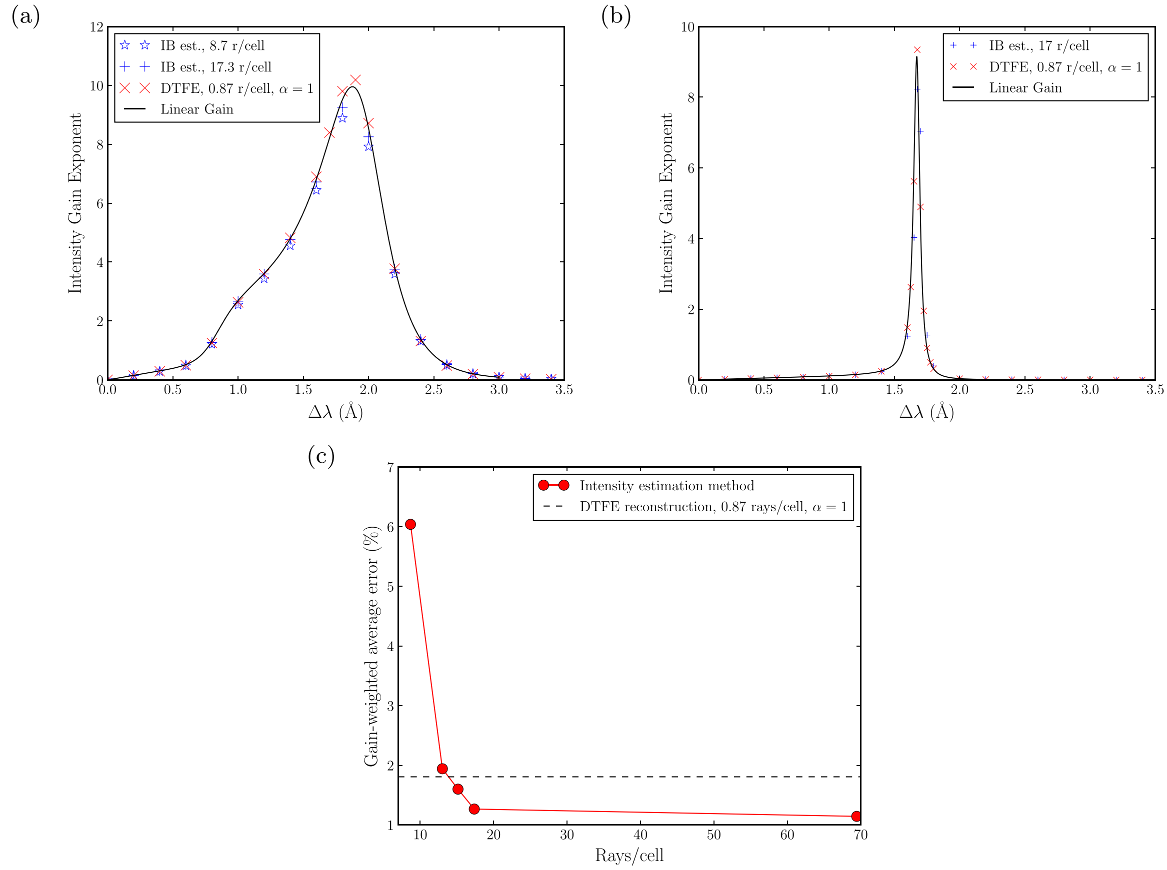

FIG. 8. Intensity gain exponent as a function of detuning between the interacting beams, for (a) a C_5H_{12} plasma at 0.15 n_c and (b) a He plasma at 0.02 n_c. Gain exponents obtained with HYDRA using inverse-bremsstrahlung intensity reconstruction and with the DTFE-based VAMPIRE code are shown as blue and red symbols, respectively. (c) Average CBET gain error scaling with the number of rays for the inverse-Bremsstrahlung intensity reconstruction method. The error obtained in the DTFE case with 0.87 rays/cell and $\alpha = 1$ is shown as a dashed black line.

$$\hat{E} = \frac{\int (G_{\rm sim} - G_{\rm th}) d\lambda}{\int G_{\rm th} d\lambda} \tag{14}$$

with $G_{\rm th}(\lambda)$ being the theoretical linear gain and $G_{\rm sim}(\lambda)$ the simulated gain. It is found that the rigid-scale method achieves with 14 rays/cell the same accuracy as the DTFE method with 0.87 rays/cell and $\alpha = 1$ (the high value of α is chosen to reproduce a smoother field, as shown in Sec. III B 1).

In contrast to reduced CBET models based on matrix exponentials or point-like exchanges between Gaussian beamlets,[9] ray-based CBET models implementing Eq. (12) do not conserve energy analytically. We have found that energy conservation in our CBET algorithm is mainly dependent on the local gain compared to the cell size along the beam propagation direction. For longitudinal resolutions of 100 μm, we have found that the algorithm conserves energy to within 1% of the total exchanged energy, for total gains up to 4.5. In typical indirect-drive NIF simulations where interaction lengths are long but local gains are rather modest, we have observed energy conservation of the order of 0.7% of the total exchanged energy when using longitudinal resolutions of up to 130 μm.

C. Comparison to an experiment and paraxial simulations for CBET in the pump depletion regime

We now compare VAMPIRE with the results obtained during the Beam Combiner experiments on NIF[30] and with reference Paraxial simulations conducted with pF3D.[31] This comparison is provided as a validation of the DTFE-PCVT approach for CBET computation with a linear kinetic response for the plasma. In a regime where (i) the detailed intensity statistics does not play a role, (ii) a sufficient number of rays per cell can be obtained, and (iii) no additional physics included in VAMPIRE plays a role (Such physics package includes the frequency shift of the beams by temporal density fluctuations and detailed beam spectra induced by Smoothing by Spectral Dispersion. These play a minor role here and will be described in a following paper.) similar results would be obtained with a CBET model based on rigid-scale estimation such as the one presented in Sec. IV B.

The experiment consists of interacting a probe beam with zero to two resonant pump quads in a uniform plasma generated with 44 heater beams. The probe beam and pump quads are detuned by 1 Å in the UV to satisfy resonance for their crossing angle of ~20°. In addition to its amplification by resonant pumps, the probe beam is also weakly amplified by the non-resonant heater beams at various angles. The CBET occurs in a non-linear regime of the instability since the pumps lose significant power during the interaction (up to ~75% of pump depletion at peak power).

The probe beam (B165 of quad Q16B) contains 0.75 kJ of energy in a 1 ns Gaussian pulse and has a quasi-flat-top elliptical intensity profile of 862 μm and 617 μm 1/e radii, corresponding to a maximum intensity of 4.7×10^{13} W/cm^2.

The pump quads have approximately constant powers around 1 TW/beam, corresponding to maximum intensities of 1.3×10^{14} and $1.5 \times 10^{14}\,\mathrm{W/cm^2}$ for Q12B and Q42B, respectively. 2D-axisymmetric hydrodynamic simulations conducted with HYDRA suggest that the heater interaction with the C_5H_{12} gas bag produces a quasi-uniform plasma at a peak probe beam power of $n_e = 0.025 n_c$, $T_e = 1.8$ keV, $T_i = 0.3$ keV, and a radius of ~6 mm. For the purpose of estimating these hydrodynamic conditions, simulations in 2D-axisymmetric geometries are sufficient since the arrangement of the heater beams is mostly axisymmetric. VAMPIRE calculations are conducted in the detailed 3D configuration. Three cases corresponding to three separate experiments are considered: (i) interaction of the probe with the non-resonant heater beams only (shot N160905-002), (ii) interaction with the pump quad Q12B with an average angle of 19.5° (shot N160208-002) in addition to the heater beams, and (iii) interaction with the two pump quads Q12B and Q42B with average angles of 19.5° and 20.7°, respectively (shot N160905-001), in addition to the heater beams.

The beams after interaction propagate to a Ta witness plate that converts the deposited energy to kilovolt x-ray photons detected by an imaging camera. A 3D representation of the beam path (without the gas bag) and of the plate as seen from the camera is shown in Fig. 9 [top].

VAMPIRE simulations are conducted assuming homogeneous plasma parameters and sampling the measured beam power profiles every 100 ps for each shot. We model each beam with 2000 rays and $\alpha = 0$ on a $150 \times 150 \times 150$ mesh spanning a domain of $0.6 \times 0.6 \times 0.6$ cm. The laser beams after the interaction region are propagated onto the witness plate, and we reproduce synthetically the plate orientation and viewing angle in 3D. The laser intensity on the plate is reconstructed using the same DTFE technique as presented in Sec. III. A comparison of the simulated post-CBET laser intensity profiles on the witness plate with the measured X-ray emission in the experiment is shown in Fig. 9 [middle, bottom]. We have assumed for simplicity a linear dependency between X-ray emission and laser intensity, which allows for a qualitative comparison of the spot shapes and positions.

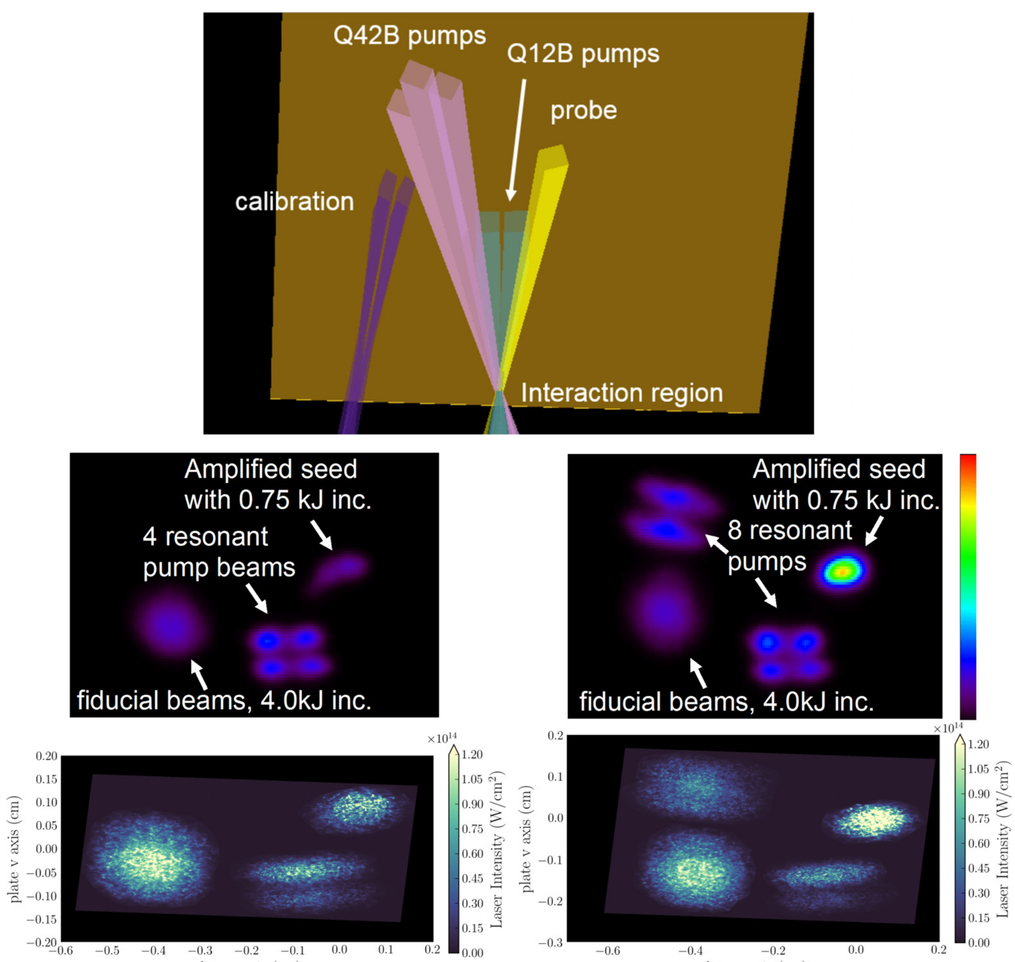

FIG. 9. [Top] Representation of the beam trajectories in vacuum in the Beam Combiner experimental configuration. The witness plate is shown in the brown and the viewing angle is that of the imaging camera. [Middle] Time-integrated X-ray images of the witness plate, calibrated to have the same brightness for the calibration spots.[30] Plots courtesy of R. Kirkwood. [Bottom] Reconstructed intensity profiles on the witness plate as viewed from the imaging camera port. Data are from VAMPIRE simulations taken at the peak power of the probe beam. The plate is positioned at a distance of $D_{\mathrm{TCC}} = 1.2$ cm from the Target Chamber Center (TCC) along the bisector of the interacting probe beam and Q12B pump quad, that is, $\zeta_{\mathrm{bisector}} = 38.5°$ and $\phi_{\mathrm{bisector}} = 246.9°$ (ζ is the polar angle, zero at the chamber north pole, and ϕ is the azimuthal angle). The plate normal is oriented along $\zeta_{\mathrm{normal}} = 32°$ and $\phi_{\mathrm{normal}} = 258°$, and the plate is viewed from a port located at $\zeta_{\mathrm{camera}} = 90°$, $\phi_{\mathrm{camera}} = 78°$.

There is qualitative agreement between the spots' relative positions and sizes between the experiments and simulations. Notably, the simulations reproduce the seed non-uniform intensity profile in the 1-pump quad case, which is due to the geometry of the interaction. The increased spot homogeneity observed in the 2-pump quad case is also reproduced by the simulations. Finally, the experiments show preferential depletion of the pumps on the two bottom beams in Q12B, which is also reproduced in the simulations. Additional simulations have shown that this effect is due to the polarization scheme for the NIF beams, which is accounted for in the code (see Sec. IV A).

Significant discrepancies are observed in the shape of the pump quads on the plate. The four beams in Q12B appear to be separated in both experiments, while the simulation produces two bands, formed by pairs of beams close together. Interestingly, the Q42B beams produce the two band pattern in the 2-pump quad experiment, while the simulation predicts a more homogeneous spot. Additional simulations with small variations in the plate position in space show that the spot shape is not sensitive to plate positioning errors, while the relative position of the spots is rather sensitive. Better agreement in that respect is observed in the 2-pump quad case with a distance from TCC increased by 500 μm. The fact that the pump beam spots does not change significantly with small variations in the plate position is related to the large Rayleigh range of the NIF beams.

Given the discrepancy observed in pump quad shapes on the witness plate, it is interesting to compare VAMPIRE results with Paraxial simulations that include more laser propagation physics. Model results are compared with numerical computations of the Beam Combiner experiments made with pF3D. The code uses the NIF phase plate data (see Fig. 4), allowing comprehensive modeling of the laser speckles and envelope in the far field, including refraction and diffraction. The paraxial approach describes the ion acoustic wave response of the plasma, leading to the CBET and backscatter from Stimulated Brillouin Scattering. Comparisons of the seed beam and pump beam spot shapes after the interaction regions between the VAMPIRE and pF3D are shown in Fig. 10. The intensity profiles in both cases have been spatially smoothed using a 2D Gaussian kernel of 75 μm standard deviation to allow for a comparison of the laser intensity envelope. Both approaches reproduce the deviation of the probe beam intensity field barycenter, as is seen in the experimental data. Both approaches are also consistent in the shape of the pump beams, with a top-down asymmetry due to beam polarizations and two ellipsoid shapes, in contrast to the experimental result.

Finally, we show in Fig. 11 a summary of the time-integrated probe beam amplification as a function of the number of pump quads. Note that the pF3D simulation does not account for the contribution from the heater beams since their angle with the probe beam is too large to remain within the paraxial approximation. For the same reason, the two pump quad case is not simulated with pF3D. There is a good overall agreement between the experimental data, VAMPIRE, and pF3D. While the predicted beam amplification in the two pump-quad case is slightly underestimated by VAMPIRE, the discrepancy is reduced when considering inhomogeneity

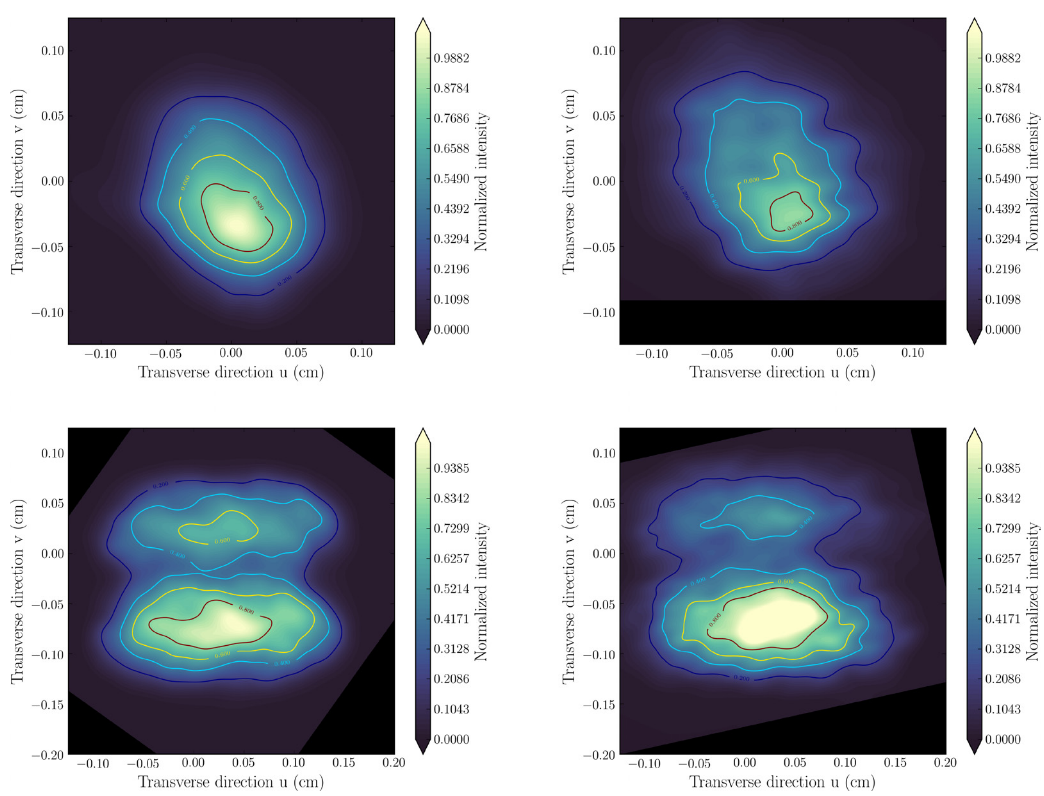

FIG. 10. Intensity slices in a plane orthogonal to the bisector between the seed beam and Q12B in the 1-pump quad case, at 1.2 cm from TCC. [Top] probe beam profiles and [bottom] pump beam profiles, from [left] pF3D simulations and [right] VAMPIRE simulations. Spot profiles have been normalized to contain the same power.

from the gas bag target. Indeed, while the center of the gasbag is expected to be rather homogeneous, the laser-target interaction produces a shock traveling toward the target center. HYDRA and VAMPIRE simulations suggest that at the time of interaction, the beams may clip the higher-density region associated with the shock, thus producing increased amounts of CBET. Finally, it is interesting to note that probe beam amplification in the absence of pumps is observed in both simulation and experiment, showing that non-resonant interactions between the probe and the heater beams also play a role.

V. CONCLUSIONS

We have developed a new ray-based laser intensity estimation method for plasmas that is not dependent on the choice of an underlying grid. In contrast to usual rigid-scale estimators that use a fixed grid to bin the contributions from GO rays, we use the ray positions themselves to estimate the local field density. This approach is particularly efficient in 3D geometries, where traditional rigid-scale estimators have poor convergence properties. The field is estimated using a modified Delaunay Triangulation tesselation estimator. This method reproduces correctly the large-scale beam parameters, including minor and major axes for elliptical beams, average intensity, and super-Gaussian order. Although the field estimator is sensitive to noise in the point distribution, laser beams smoothed by phaseplates also present some degree of intensity statistics which is comparable to what the estimator produces. This allows us to keep the number of rays low, typically 2000 per beam, thus enhancing the method efficiency while describing a realistic laser intensity field. The speckle size remains large compared to real speckle, which may be an issue when considering instabilities with a significant gain per speckle length. In order to add control on the intensity distribution, a relaxation scheme based on Penalized Centroidal Voronoi Tesselation was implemented, allowing us to change the modeled speckle size and slope of the tail of the intensity distribution.

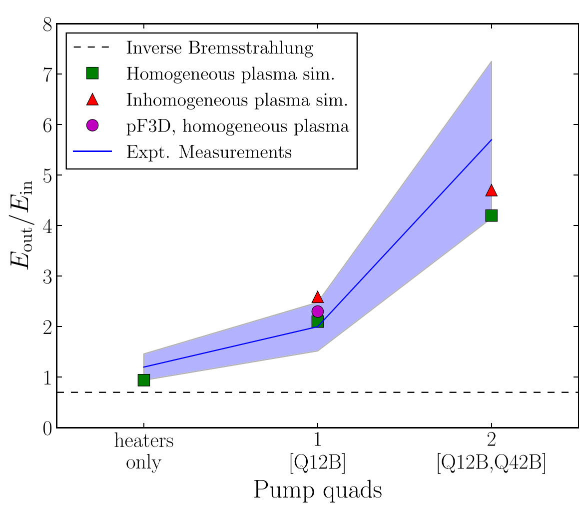

FIG. 11. Time-integrated probe beam amplification as a function of the number of pump quads. Experimental results with uncertainties are shown as a blue shaded region. Simulations with VAMPIRE are shown as green squares for the homogeneous plasma case and red triangles for the inhomogeneous case. The PF3D simulation is indicated with a magenta circle. The estimated contribution to beam damping from inverse Bremsstrahlung absorption, i.e., the *beam amplification* in the absence of CBET, is indicated as a dashed line.

A Crossed Beam Energy Transfer model has been implemented in this framework. It is based on the resolution of the steady-state plane wave equations for CBET. The effect of individual beam polarization is accounted for in the limit of weak refraction and moderate gains. The numerical implementation allows us to account for pump depletion in the case of co-propagating beams. The code has been validated against kinetic theory for linear gains. Comparison in a pump depletion regime has shown good agreement with experimental results and paraxial simulations.

The code has been implemented with the detailed 3D geometry of the NIF beams, and laser propagation is computed along 3D plasma gradients. This makes it a flexible tool for future studies on 3D hydrodynamic profiles, which are becoming more and more computationally accessible. Since the CBET is computed between all NIF beams, the code can be used to extract spatial gain rates detailing the contribution of each beam. This can in turn be used by paraxial codes as a source term to account for the contributions of beams at high angles. Furthermore, the amplification contribution from all quads to SBS and SRS backscattered light can be computed. This will allow us in the future to compute realistic SBS and SRS backscatter maps on the NIF chamber walls and reproduce synthetic FABS diagnostics. A TPD module is also under development, to enhance the predictive capabilities for hot electron production and propagation in the holhraum.

ACKNOWLEDGMENTS

This work was performed under the auspices of the U.S. Department of Energy by Lawrence Livermore National Laboratory under Contract No. DE-AC52-07NA27344.

APPENDIX: CBET NUMERICAL SCHEME

The implementation of the GO algorithm in the code described in this paper uses hydrodynamic quantities defined at mesh nodes and tri-linearly interpolated inside each 3D cell. Following this scheme, the CBET coupling coefficients Γ_n are also computed at the mesh nodes and tri-linearly interpolated within each cell. This requires us to sample the laser field related quantities (k-vectors, frequency, and intensity) at the nodes. This is done in the same way for the 5 quantities of interest (k_x, k_y, k_z, ω, and I): (i) the beam parameters known at the $\mathcal{M}_z$ positions are sampled on a high resolution grid using bi-linear interpolation within each Delaunay triangle, (ii) the parameters are then binned (using an average statistics) onto 2D cells which barycenters coincide with the hydrodynamic mesh. Similar to the scheme detailed in Sec. III, a sharp cutoff is used such that cells outside the convex hull of each beam are associated with a null value. Note that instead of relying on a grid common to all beams to compute a transfer coefficient summed over all beams, we could use directly the beam point distributions to compute beam by

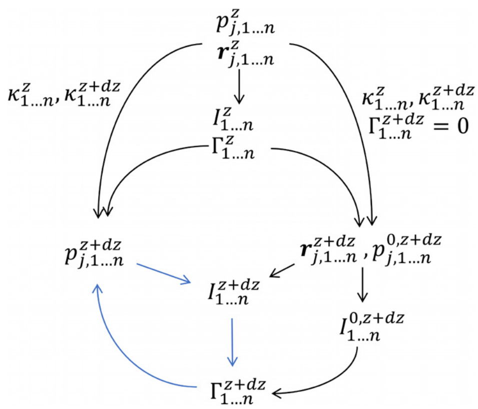

FIG. 12. Iterating scheme used to solve Eq. (12) for N fields between $\mathcal{P}_z$ and $\mathcal{P}_{z+dz}$, allowing us to include refraction effects. The initialization step is shown in black and the iteration step in blue. **r** denotes the ray positions, p the ray powers, I the beam intensity field, κ the inverse Bremsstrahlung absorption field (known prior to computation from the hydrodynamic quantities), and Γ the CBET coupling coefficient.

beam coupling coefficients at ray locations. This would likely increase the algorithm efficiency and may be considered in the future.

The system of equations on the N wavefields (12) can be solved analytically using matrix exponentials in the absence of refraction. The situation is more complex in the presence of laser refraction: the laser intensity field at step z + dz contains a component that originates from the convergence or divergence of ray tubes and the contribution of adjacent rays, and the z coordinate in Eq. (12) becomes curvilinear. For simplicity, we solve Eq. (12) with an iterating scheme between planes $\mathcal{P}_z$ and $\mathcal{P}_{z+dz}$ at coordinates z and z + dz (see Fig. 12):

1. the laser intensity of the N fields is computed from $\mathcal{M}_z$,
2. rays are traced from z to $z+dz$ accounting for inverse Bremsstrahlung absorption [κ_n in (12)] and half of the contribution from CBET ($\Gamma_n \neq 0$ for nodes at z and $\Gamma_n = 0$ for nodes at $z+dz$),
3. the laser intensity is computed in $\mathcal{P}_{z+dz}$ from $\mathcal{M}_{z+dz}$ and the ray powers, thus accounting for absorption, refraction, and part of the CBET,
4. Γ_n is computed at the mesh nodes in $\mathcal{P}_{z+dz}$ using the estimated intensity in the previous step,
5. knowing the values of Γ_n and κ_n at the nodes of both $\mathcal{P}_z$ and $\mathcal{P}_{z+dz}$, Eq. (12) is re-integrated along ray trajectories,
6. the intensity field in $\mathcal{P}_{z+dz}$ is recomputed.

The last two steps can be re-iterated to ensure numerical convergence, which is typically observed after one iteration for the modest gains of interest in our cases ($G \ll 1$ per dz unit length). Numerical integration of Eq. (12) is conducted using the LSODA[32] integrator, which switches automatically between stiff and non-stiff methods on the fly. This has been observed as useful in cases of sharp spatial resonances in Γ.

[1]J. D. Lindl, P. Amendt, R. L. Berger, S. Gail Glendinning, S. H. Glenzer, S. W. Haan, R. L. Kauffman, O. L. Landen, and L. J. Suter, "The physics basis for ignition using indirect-drive targets on the national ignition facility," Phys. Plasmas **11**(2), 339–491 (2004).
[2]S. H. Glenzer, D. H. Froula, L. Divol, M. Dorr, R. L. Berger, S. Dixit, B. A. Hammel, C. Haynam, J. A. Hittinger, J. P. Holder, O. S. Jones, D. H. Kalantar, O. L. Landen, A. B. Langdon, S. Langer, B. J. MacGowan, A. J. Mackinnon, N. Meezan, E. I. Moses, C. Niemann, C. H. Still, L. J. Suter, R. J. Wallace, E. A. Williams, and B. K. F. Young, "Experiments and multiscale simulations of laser propagation through ignition-scale plasmas," Nat. Phys. **3**(10), 716–719 (2007).
[3]I. V. Igumenshchev, D. H. Edgell, V. N. Goncharov, J. A. Delettrez, A. V. Maximov, J. F. Myatt, W. Seka, A. Shvydky, S. Skupsky, and C. Stoeckl, "Crossed-beam energy transfer in implosion experiments on omega," Phys. Plasmas **17**(12), 122708 (2010).
[4]P. Michel, L. Divol, E. A. Williams, S. Weber, C. A. Thomas, D. A. Callahan, S. W. Haan, J. D. Salmonson, S. Dixit, D. E. Hinkel, M. J. Edwards, B. J. MacGowan, J. D. Lindl, S. H. Glenzer, and L. J. Suter, "Tuning the implosion symmetry of icf targets via controlled crossed-beam energy transfer," Phys. Rev. Lett. **102**(2), 025004 (2009).
[5]D. Batani, S. Baton, A. Casner, S. Depierreux, M. Hohenberger, O. Klimo, M. Koenig, C. Labaune, X. Ribeyre, C. Rousseaux, G. Schurtz, W. Theobald, and V. T. Tikhonchuk, "Physics issues for shock ignition," Nucl. Fusion **54**(5), 054009 (2014).
[6]T. B. Kaiser, "Laser ray tracing and power deposition on an unstructured three-dimensional grid," Phys. Rev. E **61**, 895 (2000).
[7]Y. A. Kravtsov and N. Y. Zhu, *Theory of Diffraction, Heuristic Approaches*, Alpha science series on wave phenomena (Alpha Science International LTD., Oxford, U.K., 2010).
[8]J. A. Marozas and T. J. B. Collins, "Cross-beam energy transfer (cbet) effect with additional ion heating integrated into the 2-d hydrodynamics code draco," in Proceedings of the APS Meeting Abstracts, October (2012), p. 5003.
[9]A. Colaïtis, G. Duchateau, X. Ribeyre, and V. Tikhonchuk, "Modeling of the cross-beam energy transfer with realistic inertial-confinement-fusion beams in a large-scale hydrocode," Phys. Rev. E **91**, 013102 (2015).
[10]A. Colaïtis, G. Duchateau, X. Ribeyre, Y. Maheut, G. Boutoux, L. Antonelli, Ph. Nicolaï, D. Batani, and V. Tikhonchuk, "Coupled hydrodynamic model for laser-plasma interaction and hot electron generation," Phys. Rev. E **92**, 041101 (2015).
[11]D. J. Strozzi, D. S. Bailey, P. Michel, L. Divol, S. M. Sepke, G. D. Kerbel, C. A. Thomas, J. E. Ralph, J. D. Moody, and M. B. Schneider, "Interplay of laser-plasma interactions and inertial fusion hydrodynamics," Phys. Rev. Lett. **118**, 025002 (2017).
[12]A. Colaïtis, G. Duchateau, P. Nicolaï, and V. Tikhonchuk, "Towards modeling of nonlinear laser-plasma interactions with hydrocodes: The thick-ray approach," Phys. Rev. E **89**, 033101 (2014).
[13]Y. A. Kravtsov and P. Berczynski, "Gaussian beams in inhomogeneous media: A review," Stud. Geophys. Geod. **51**, 1–36 (2007).
[14]Y. A. Kravtsov, "Complex rays and complex caustics," Radiophys. Quantum Electron. **10**, 719–730 (1967).
[15]M. A. Aragón-Calvo, B. J. T. Jones, R. van de Weygaert, and J. M. van der Hulst, "The multiscale morphology filter: Identifying and extracting spatial patterns in the galaxy distribution," Astron. Astrophys. **474**(1), 315–338 (2007).
[16]E. Platen, R. Van De Weygaert, and B. J. T. Jones, "A cosmic watershed: The wvf void detection technique," Mon. Not. R. Astron. Soc. **380**(2), 551–570 (2007).
[17]V. J. Martínez, J.-L. Starck, E. Saar, D. L. Donoho, and S. C. Reynolds, "Pablo de la Cruz, and Silvestre Paredes. Morphology of the galaxy distribution from wavelet denoising," Astrophys. J. **634**(2), 744 (2005).
[18]M. A. Aragón-Calvo, E. Platen, R. van de Weygaert, and A. S. Szalay, "The spine of the cosmic web," Astrophys. J. **723**(1), 364 (2010).
[19]E. Platen, R. van de Weygaert, B. J. T. Jones, G. Vegter, and M. A. Aragón Calvo, "Structural analysis of the sdss cosmic web—i. Non-linear density field reconstructions," Mon. Not. R. Astron. Soc. **416**(4), 2494–2526 (2011).
[20]W. E. Schaap, "DTFE: The delaunay tessellation field estimator," Ph.D. thesis (University of Groningen, 2007).
[21]M. Browne, "A geometric approach to non-parametric density estimation," Pattern Recognit. **40**(1), 134–140 (2007).
[22]H. A. Rose and D. F. DuBois, "Statistical properties of laser hot spots produced by a random phase plate," Phys. Fluids B **5**, 590–596 (1993).
[23]J. Garnier, "Statistics of the hot spots of smoothed beams produced by random phase plates revisited," Phys. Plasmas **6**, 1601–1610 (1999).
[24]P. Michel, L. Divol, E. A. Williams, C. A. Thomas, D. A. Callahan, S. Weber, S. W. Haan, J. D. Salmonson, N. B. Meezan, O. L. Landen, S. Dixit, D. E. Hinkel, M. J. Edwards, B. J. MacGowan, J. D. Lindl, S. H.

Glenzer, and L. J. Suter, "Energy transfer between laser beams crossing in ignition holhraums," Phys. Plasmas **16**(4), 042702 (2009).
[25]G. Cristoforetti, A. Colaïtis, L. Antonelli, S. Atzeni, F. Baffigi, D. Batani, F. Barbato, G. Boutoux, R. Dudzak, P. Koester, E. Krousky, L. Labate, Ph. Nicolaï, O. Renner, M. Skoric, V. Tikhonchuk, and L. A. Gizzi, "Experimental observation of parametric instabilities at laser intensities relevant for shock ignition," Europhys. Lett. **117**(3), 35001 (2017).
[26]D. Pesme, G. Bonnaud, M. Casanova, R. Dautray, C. Labaune, G. Laval, L. Bergé, and J. P. Watteau, *La fusion thermonucléaire inertielle par laser: l'interaction laser-matière part. 1*, French ed. (Synthèses Eyrolles, 61, Boulevard, Saint-Germain, 1993).
[27]P. Michel, W. Rozmus, E. A. Williams, L. Divol, R. L. Berger, S. H. Glenzer, and D. A. Callahan, "Saturation of multi-laser beams laser-plasma instabilities from stochastic ion heating," Phys. Plasmas **20**(5), 056308 (2013).
[28]D. J. Strozzi, E. A. Williams, D. E. Hinkel, D. H. Froula, R. A. London, and D. A. Callahan, "Ray-based calculations of backscatter in laser fusion targets," Phys. Plasmas **15**(10), 102703 (2008).
[29]M. M. Marinak, G. D. Kerbel, N. A. Gentile, O. Jones, D. Munro, S. Pollaine, T. R. Dittrich, and S. W. Haan, "Three-dimensional hydra simulations of national ignition facility targets," Phys. Plasmas **8**(5), 2275–2280 (2001).
[30]R. K. Kirkwood, D. P. Turnbull, T. Chapman, S. C. Wilks, M. D. Rosen, R. A. London, L. A. Pickworth, W. H. Dunlop, J. D. Moody, D. J. Strozzi, P. A. Michel, L. Divol, O. L. Landen, B. J. MacGowan, B. M. Van Wonterghem, K. B. Fournier, and B. E. Blue, "Plasma-based beam combiner for very high fluence and energy," Nat. Phys. **14**, 80–84 (2017).
[31]R. L. Berger, C. H. Still, E. A. Williams, and A. B. Langdon, "On the dominant and subdominant behavior of stimulated raman and brillouin scattering driven by nonuniform laser beams," Phys. Plasmas **5**(12), 4337–4356 (1998).
[32]A. C. Hindmarsh, "Odepack, a systematized collection of ode solvers," Sci. Comput. **1**, 55–64 (1983).
[33]The inverse-Bremsstrahlung based estimator can be refined by assuming linearly varying parameters in the volume when gradients are present. The conclusions presented in this paper are not affected by such refinement since only homogeneous plasmas are considered for comparison purposes.
[34]We compute the complex Z function of purely real argument (from the beating of the two relevant light waves), using a rational function fit for $\Re(Z)$ and the exact expression for $\Im(Z)$.
[35]G. Kerbel, private communication (2017).